Open access • Journal Article • DOI:10.1103/PHYSREVLETT.103.257603

Optical control of field-emission sites by femtosecond laser pulses.

Hirofumi Yanagisawa, Christian Hafner, Patrick Doná, Martin Klöckner ...+4 more authors

Institutions: University of Zurich, ETH Zurich

Published on: 17 Dec 2009 - Physical Review Letters (American Physical Society)

Topics: Laser, Femtosecond, Field electron emission and Ultrashort pulse

Optical control of field-emission sites by femtosecond laser pulses

Yanagisawa, H; Hafner, C; Doná, P; Klöckner, M; Leuenberger, D; Greber, T; Hengsberger, M; Osterwalder, J

Optical control of field-emission sites by femtosecond laser pulses

Abstract

We have investigated field-emission patterns from a clean tungsten tip apex induced by femtosecond laser pulses. Strongly asymmetric modulations of the field-emission intensity distributions are observed depending on the polarization of the light and the laser incidence direction relative to the azimuthal orientation of tip apex. In effect, we have realized an ultrafast pulsed field-emission source with site selectivity. Simulations of local fields on the tip apex and of electron emission patterns based on photoexcited nonequilibrium electron distributions explain our observations quantitatively.

Optical Control of Field-Emission Sites by Femtosecond Laser Pulses

Hirofumi Yanagisawa[1],* Christian Hafner[2], Patrick Doná[1], Martin Klöckner[1], Dominik Leuenberger[1], Thomas Greber[1], Matthias Hengsberger[1], and Jürg Osterwalder[1]
[1] *Physik Institut, Universität Zürich, Winterthurerstrasse 190, CH-8057 Zürich, Switzerland*
[2] *Laboratory for Electromagnetic Fields and Microwave Electronics, ETH Zürich, Gloriastrasse 35, CH-8092 Zürich, Swizerland*
(Dated: September 29, 2009)

We have investigated field emission patterns from a clean tungsten tip apex induced by femtosecond laser pulses. Strongly asymmetric modulations of the field emission intensity distributions are observed depending on the polarization of the light and the laser incidence direction relative to the azimuthal orientation of tip apex. In effect, we have realized an ultrafast pulsed field-emission source with site selectivity. Simulations of local fields on the tip apex and of electron emission patterns based on photo-excited nonequilibrium electron distributions explain our observations quantitatively.

PACS numbers: 79.70.+q, 73.20.Mf, 78.47.J-, 78.67.Bf

Applying strong electric fields to a metal enables field emission due to electron tunneling into the vacuum. Field emission from metallic tips with nanometer sharpness is particularly interesting due to the high brightness and coherence of the electron beams [1–6]. When a focused pulsed laser illuminates the tip, optical electric fields are enhanced at the tip apex (*local field enhancement*) due to the excitation of surface electromagnetic (EM) waves like, e.g., surface plasmon polaritons. Only recently, it was found that the enhanced fields induce pulsed field emission in combination with a moderate DC voltage applied to the tip [7–10]. Depending on the strength of the enhaced field, different field emission processes become dominant [7]. For relatively weak fields, single electron excitations by single- or multiphoton absorption are prevalent, and photo-excited electrons are tunneling through the surface potential barrier (*photo-field emission*). On the other hand, very strong fields largely modify the tunneling barrier and prompt the field emission directly (*optical field emission*).

So far, the different emission processes were disputed in the literature, while the local field enhancement was treated as a static effect of the laser field such as the lightening rod effect [7, 8, 11, 12]. However, dynamical effects are predicted to occur when the tip size is larger than approximately a quarter wavelength [13]. Here we used a tip whose apex was approximately a quarter wavelength, and found that dynamical effects substantially influence the symmetries of field emission intensity distributions. Varying the laser polarization changes these distributions substantially, an effect that had not been observed in earlier experiments [7, 14]. At the same time, we have realized an ultrafast pulsed electron source with emission site selectivity of a few ten nanometers, improving thus on values reached in previous work based on polarization shaped laser pulses impinging on nanostructures [15]. Simulations of local fields on the tip apex and of electron emission patterns based on the photo-field emission model describe our observations quantitatively.

Fig. 1 schematically illustrates our experimental setup. A tungsten tip with its axis along the (011) crystal direction is mounted inside a vacuum chamber ($3 \cdot 10^{-10}$ $mbar$). Laser pulses are generated in a Ti:sapphire oscillator (wave length: 800 nm; repetition rate: 76 MHz; pulse width: 55 fs; average laser power P_L: 20 mW) and introduced into the vacuum chamber. The laser light was focused to 4 μm ($1/e^2$ radius) onto the tip apex. Linearly polarized laser light was used. The polarization vector can be changed within the transversal (x, z) plane by using a $\lambda/2$ plate. As shown in the inset, where the laser propagates towards the reader's eye as denoted by the red mark, the polarization angle θ_P is defined by the angle between the tip axis and the polarization vector. The tip can be heated to clean the apex and also negatively biased for field emission. A position-sensitive detector in front of the tip measures the emission patterns. The

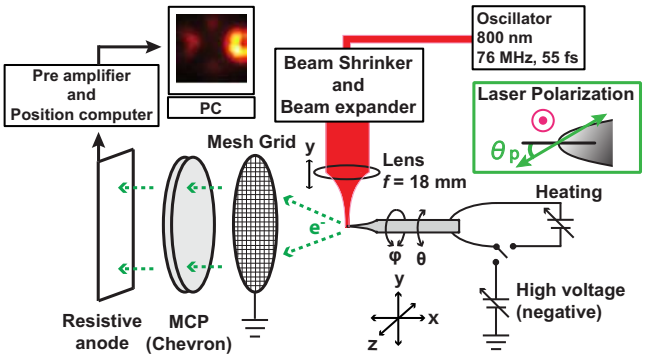

FIG. 1: Schematic diagram of the experimental setup. A tungsten tip is mounted inside a vacuum chamber. Laser pulses are generated outside the vacuum chamber. An aspherical lens is located just next to the tip to focus the laser onto the tip apex. Emitted electrons are detected by a position-sensitive detector in front of the tip. The polarization angle θ_P is defined in the inset, where the laser beam propagates towards the reader's eye (see text for further description).

*Electronic address: hirofumi@physik.uzh.ch

spatial resolution of field emission microscopy (FEM) is approximately 3 nm [1]. The tip holder can move along three linear axes (x, y, z) and has two rotational axes for azimuthal (φ, around the tip axis) and polar (θ, around the z axis) angles. θ is set so that the tip axis is orthogonal to the laser propagation axis with a precision of $\pm$ 1 degree, and the laser propagates parallel to the horizontal y axis within an error of $\pm$ 1 degree. In these experiments, the base line of the rectangular detector is approximately 20° off from the horizontal (y axis) incidence direction, which means that the laser propagation axis is inclined by 20° from the horizontal line in the observed laser-induced FEM images (see dashed red arrow in Fig. 2a).

The field emission pattern from the clean tungsten tip is shown in Fig. 2(a) where the most intense electron emission is observed around the (310)-type facets, and weaker emission from (111)-type facets. These regions are highlighted by green areas on the schematic front view of the tip apex in the inset of Fig. 2(a). The intensity map roughly represents a work function map of the tip apex: the lower the work function is, the more electrons are emitted. The relatively high work functions of (011)- and (001)-type facets [16] suppress the field emission from those regions.

The laser-induced FEM (LFEM) image in Fig. 2(b), taken with the light polarization oriented parallel to the tip axis ($\theta_P = 0$), shows a striking difference in symmetry compared to that of the FEM image in Fig. 2(a). Emission sites are the same in both cases, but the emission pattern becomes strongly asymmetric with respect to the shadow (right) and exposed (left) sides relative to the laser incidence direction. The most intense emission is observed on the shadow side as illustrated in the inset of Fig. 2(b). Actually, the laser pulses arrive at an oblique angle as indicated by the dashed red arrow in the inset of Fig. 2(a), which slightly affects the symmetry with respect to the central horizontal line in the observed LFEM images (see below).

We found experimentally a strong dependence of the electron emission patterns on the laser polarization direction and azimuthal tip orientation. Fig. 3 shows the LFEM patterns for different values of θ_P in 30° steps,

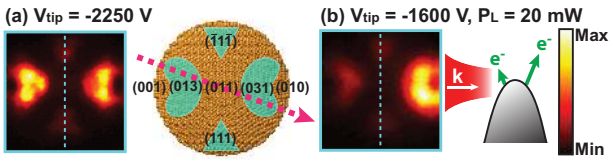

FIG. 2: Electron emission patterns without laser (a), and with laser irradiation (b). V_{tip} indicates the DC potential applied to the tip and P_L indicates the laser power measured outside the vacuum chamber. The inset of (a) shows the front view of the atomic structure of a tip apex based on a ball model. The inset of (b) shows a schematic side view of the laser-induced field emission geometry. A dashed blue line denotes a mirror symmetry line of the atomic structure in each picture.

and for four different azimuthal orientations φ of the tip. The corresponding FEM images are also shown in the left-most column. Throughout the whole image series, emission sites do not change, but intensities are strongly modulated resulting in highly asymmetric features.

When a laser pulse illuminates the metallic tip, surface EM waves [17] are excited, which propagate around the tip apex as illustrated schematically in Fig. 4(a). Due to the resulting interference pattern, the electric fields show an asymmetric distribution over the tip apex, depending also on the laser polarization. To simulate the propagation of these surface EM waves and the resulting field distributions, we used the software package MaX-1 for solving Maxwell equations based on the Multiple Multipole Program [19]. A droplet-like shape was employed as a model tip as shown in Fig. 4(b), with a radius of curvature of the tip apex of 100 nm, which is a typical value for a clean tungsten tip. The dielectric function ϵ of tungsten at 800 nm was used: a real part $\Re(\epsilon) = 5.2$ and an imaginary part $\Im(\epsilon) = 19.4$ [20]. By using different droplet sizes it was verified that the model tip is long enough so as to mimick the infinite length of the real tip.

Fig. 4(b) shows the calculated time-averaged field distribution over a cross section of the model tip, where the polarization vector has been chosen parallel to the tip axis ($\theta_P = 0°$). The laser propagates from left to right, and was focused at the tip apex. The field distribution is clearly asymmetric with respect to the tip axis, with a maximum on the shadow side of the tip. This is consistent with our observations in Fig. 2(b) where the field emission is enhanced on the shadow side. Fig. 4(c) shows, in a front view, time-averaged field distribution maps from the white dashed line region of the model tip in Fig. 4(b). This area corresponds roughly to the observed area in our experiments. The field distribution changes strongly depending on the polarization angle. Note that the positions of the maximum local fields are almost the same for wave lengths in the range between 750 nm and 850 nm, therefore the simulation at the center frequency of the pulse alone (800 nm) is sufficient.

From the calculated local fields, we further simulated the LFEM images by considering the photo-field emission mechanism. The current density j_{calc} of field emission can be described in the Fowler-Nordheim theory based on the free-electron model as follows [1, 2, 21, 22],

$$j_{calc} = \frac{em}{2\pi^2\hbar^3} \int_{-W_a}^{\infty} \int_{-W_a}^{W=E} D(W,\Phi,F) f(E)\, dW\, dE. \quad (1)$$

Here, e is the electron charge and m the electron mass, $-W_a$ is the effective constant potential energy inside the metal, W is the normal energy with respect to the surface, and E is the total energy. Important factors are $D(W,\Phi,F)$ and $f(E)$. $D(W,\Phi,F)$ is the probability that an electron with the normal energy W penetrates the surface barrier. It depends exponentially on the triangular-shaped potential barrier above W, as indicated in Fig. 4(d), which is determined by the work function Φ and

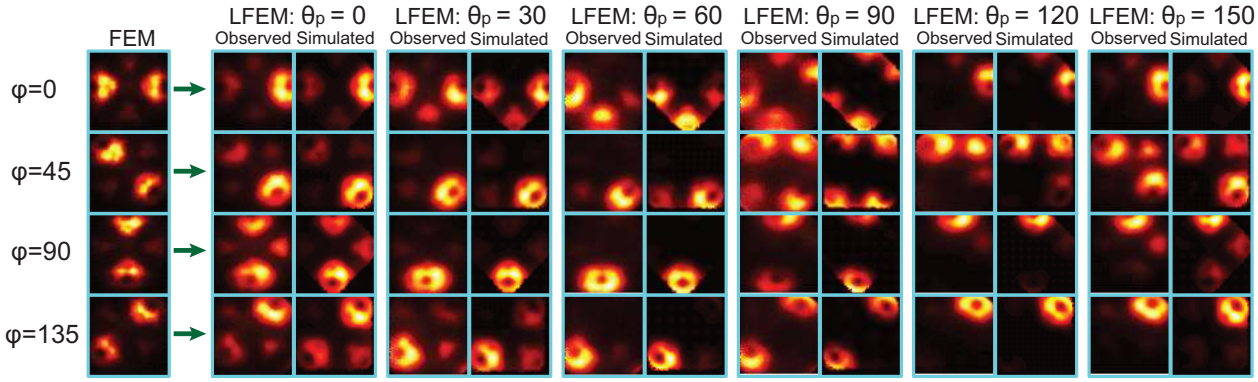

FIG. 3: Comparison of measured and simulated laser-induced FEM (LFEM) images for different light polarization angles θ_P and for different azimuthal orientations φ of the tip. The leftmost column gives the FEM images without laser irradiation for four different azimuthal angles (V_{tip} = -2250 V). For the same azimuthal angles, observed LFEM images are shown as a function of polarization angle θ_P in 30° steps ($V_{tip} \approx$ -1500 V and P_L = 20 mW). The simulated LFEM images from the photo-field emission model, in which V_{tip} and P_L were set as in the corresponding experiments, are shown on the right-hand side of the observed LFEM images. The color scale and laser propagation direction are the same as in Fig. 2.

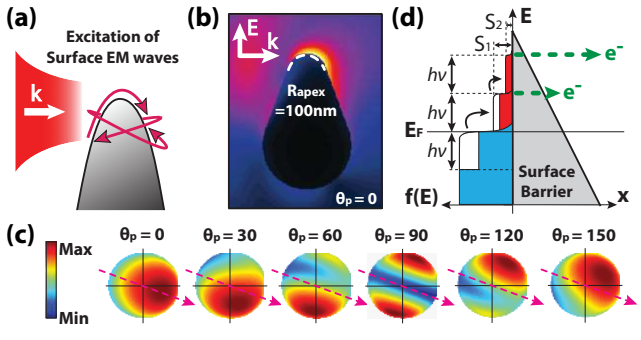

FIG. 4: Schematic illustration of the excitation and interference of surface EM waves (a). The calculated time-averaged field distribution around the model tip is shown in a linear color scale in (b) for $\theta_P = 0°$. Highest field values are represented in yellow. In (c) the time-averaged field distributions are given in a front view of the model tip for different polarization directions θ_P. The laser propagation direction is indicated by red arrows, it is the same as in the experiment. (d) shows a schematic diagram of photo-field emission from a nonequilibrium electron distribution.

the electric field F just outside the surface. $f(E)$ is an electron distribution function. In the case of field emission we have $F = F_{DC}$, where F_{DC} is the applied DC electric field, and $f(E)$ is the Fermi-Dirac distribution for an equilibrium state at a temperature of $300K$.

In the photo-field emission model, F still equals F_{DC}, but the electron distribution is strongly modified by the electron-hole pair excitations due to single- and multi-photon absorption, resulting in a nonequilibrium distribution characterized by a steplike profile, as illustrated in Fig. 4(d) [23, 24]. For example, one-photon absorption creates a step of height S_1 from E_F to $E_F+h\nu$ by exciting electrons from the region $E_F - h\nu$ to E_F. Absorption of a second photon creates a step of height S_2 from $E_F+h\nu$ to $E_F + 2h\nu$, where $S_2 = S_1^2$. We included absorption of up to four photons. The step height S_1 is proportional to the light intensity I. In the vicinity of the tip we have $I \propto F_{laser}^2$ where F_{laser} is the enhanced optical electric field that varies over the tip apex as illustrated in Fig. 4(c) [25].

There are three adjustable parameters in our calculations of j_{calc}: Φ, F, and S_1. They are all functions of position on the tip apex. Φ and F maps on the tip apex were obtained from the measured FEM images in the following way: a relative F distribution was generated by MaX-1. We then obtained the Φ map by inserting F into Eq. (1) and fitting j_{calc} to the symmetrized experimental FEM current density j_{exp}. The resulting Φ map was compared to known values for several surface facets of tungsten, and the absolute values were adjusted by multiplying the F distribution with a constant factor. Thus, a full Φ map and absolute values for F were obtained. The resulting Φ values are approximately 4.9 eV, 4.6 eV and 4.45 eV for (011), (001) and (310) surfaces, respectively, which are in fair agreement with known values [16, 26]. A field strength F of 2.25 V/nm results at the tip apex center for the FEM image taken with $V_{tip} = -2250$ V, which is a typical value for FEM. The LFEM experiments were carried out with a reduced tip voltage $V_{tip} \approx -1500V$, hence we used a scaled-down value of 1.5 V/nm in the LFEM simulations.

Substituting the obtained Φ and F distribution maps into Eq. (1), and using a nonequilibrium electron distribution $f(E)$, the absolute values of S_1 over the tip apex was determined by fitting the measured total current from the (310) facet on the right-hand side of the LFEM image in Fig. 2(b). The resulting maximum value for S_1 was $2.5 \cdot 10^{-6}$. By substituting all the adjusted parameters into Eq. (1), we could simulate all the LFEM images. The calculated current densities on the tip apex were projected to the flat screen by following the static field lines. The simulated images can now be directly compared to the experimental images (Fig. 3): they are

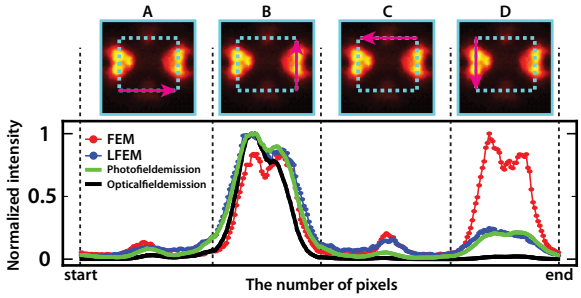

FIG. 5: Line profiles extracted from the observed FEM images (red line with dots), LFEM images (blue line with dots), and from LFEM images simulated by the photo-field emission model (green line) and the optical field emission model (black line) at $[\varphi = 0°, \theta_P = 0°]$. The whole scanned line corresponds to the unfolded rectangle indicated by the dashed blue line in the FEM figures above, and the corresponding sides are indicated by red arrows. Each line profile has been normalized by the maximum value.

in excellent agreement in every detail. This comparison clearly demonstrates that the observed strongly asymmetric features originate from the modulation of the local photo-fields. The two-photon excitations strongly dominate the emission current due to the thin barrier width (Fig. 4(d)), even though the step height S_2 is very small.

Finally, we simulated the LFEM images also for the optical field emission process and compared the resulting intensity distributions with those of the photo-field emission model. In the optical field emission model, the Fermi-Dirac distribution is not modified, but instead the electric field F in Eq. (1) is expressed as $F = F_{DC} + F^{\perp}_{laser}$ where $F^{\perp}_{laser}$ is the normal component of F_{laser}. The absolute values for $F^{\perp}_{laser}$ on the tip apex were determined in the same way as described above for the S_1 values. The resulting maximum value for $F^{\perp}_{laser}$ was 0.68 V/nm.

Fig. 5 shows line profiles extracted from the observed FEM and LFEM images, and from the corresponding simulations for both photo-field emission and optical field emission models at $[\varphi = 0°, \theta_P = 0°]$, which were all normalized by their maximum value. The whole scanned line corresponds to the unfolded rectangle indicated in the example FEM image; it provides sections through all major intensity features of these data. The measured LFEM profile clearly shows the asymmetric feature as seen in the regions B and D. The photo-field emission model (green line) catches this asymmetry much more quantitatively than the optical field emission model (black line), as can be best seen in region D. Therefore, the local fields in our experiment are still weak enough such that the photo-field emission process is the dominant one.

In summary, we have demonstrated the realization of an ultrafast pulsed field-emission source with convenient control of nanometer sized emission sites by the laser polarization and incident laser angle relative to the azimuthal orientations. The photo-field emission model reproduces our observations well. Maybe the most interesting applications will arise when two laser pulses with different polarizations or paths are used. Electron emission from two independent sources but originating from the same quantum state could be studied [5, 6]. This should create new opportunities for addressing fundamental questions in quantum mechanics such as anti-correlation of electron waves in vacuum [27], or for new directions in electron holography [28].

We acknowledge many useful discussions with Prof. H. W. Fink, Dr. T. Ishikawa, and Dr. K. Kamide. This work was supported in part by the Japan Society for the Promotion of Science (JSPS), and the Swiss National Science Foundation (SNSF).

[1] R. Gomer, "Field Emission and Field Ionization", American Institute of Physics, New York, (1993).
[2] G. Fursey, "Field Emission in Vacuum Microelectronics", Kluwer Academic / Plenum Publishers, New York, (2003).
[3] H. W. Fink, IBM. J. Res. Develop. **30**, 460 (1986).
[4] T-Y. Fu *et al.*, Phys. Rev. B **64**, 113401 (2001).
[5] B. Cho *et al.*, Phys. Rev. Lett. **92**, 246103 (2004).
[6] C. Oshima *et al.*, Phys. Rev. Lett. **88**, 038301 (2002).
[7] P. Hommelhoff *et al.*, Phys. Rev. Lett. **96**, 077401 (2006).
[8] P. Hommelhoff *et al.*, Phys. Rev. Lett. **97**, 247402 (2006).
[9] C. Ropers *et al.*, Phys. Rev. Lett. **98**, 043907 (2007).
[10] B. Barwick *et al.*, New Journal of Physics **9**, 142 (2007).
[11] L. Novotny, J. Am. Ceram. Soc. **85**, 1057-1060 (1997).
[12] B. Hecht, L. Novotny, "Principles of Nano-Optics", Cambridge University Press, Cambridge, (2005).
[13] Y. C. Martin *et al.*, J. Appl. Phys. **89**, 5774 (2001).
[14] Y. Gao *et al.*, Phys. Rev. B **35**, 4284 (1987).
[15] M. Aeschlimann *et al.*, Nature **446**, 301 (2007).
[16] C. Kittel, "Introduction to Solid State Physics" (John Wiley & Sons, New York, ed. 8, 2005).
[17] Surface EM waves are classified in terms of the dielectric functions of the material. If $\Re(\epsilon)$ is negative, then the surface EM waves are proper *surface plasmon polaritons*. On the other hand, if $\Re(\epsilon)$ is positive and $\Im(\epsilon)$ is large, the term *Zenneck waves* is more appropriate. Since they represent the same concept in the sense of the EM waves coupling with the surface charges [18], we shall use the term *surface EM waves*.
[18] F. Yang *et al.*, Phys. Rev. B **44**, 5855 (1991).
[19] http://alphard.ethz.ch/.
[20] http://www.sspectra.com/sopra.html.
[21] E. L. Murphy *et al.*, Phys. Rev. **102**, 1464 (1956).
[22] R. D. Young, Phys. Rev. **113**, 110 (1959).
[23] L. Wu *et al.*, Phys. Rev. B **78**, 224112 (2008).
[24] M. Lisowski *et al.*, Appl. Phys. A **78**, 165 (2004).
[25] M. Merschdorf *et al.*, Phys. Rev. B **70**, 193401 (2004).
[26] C. E. Mendenhall *et al.*, Phys. Rev. **51**, 346 (1937).
[27] H. Klesel *et al.*, Nature **418**, 392 (2002).
[28] A. Tonomura, Rev. Mod. Phys. **59**, 639 (1987).